Volume 1 | Number 1 | Jan 2013 | Pages 1–100

PCCP

Physical Chemistry Chemical Physics
www.rsc.org/pccp

ROYAL SOCIETY OF CHEMISTRY

This is an *Accepted Manuscript*, which has been through the Royal Society of Chemistry peer review process and has been accepted for publication.

Accepted Manuscripts are published online shortly after acceptance, before technical editing, formatting and proof reading. Using this free service, authors can make their results available to the community, in citable form, before we publish the edited article. We will replace this *Accepted Manuscript* with the edited and formatted *Advance Article* as soon as it is available.

You can find more information about *Accepted Manuscripts* in the **Information for Authors**.

Please note that technical editing may introduce minor changes to the text and/or graphics, which may alter content. The journal's standard **Terms & Conditions** and the **Ethical guidelines** still apply. In no event shall the Royal Society of Chemistry be held responsible for any errors or omissions in this *Accepted Manuscript* or any consequences arising from the use of any information it contains.

www.rsc.org/pccp

Physical Chemistry Chemical Physics

Dynamic Article Links ▶

ARTICLE TYPE

Physical Chemistry Chemical Physics Accepted Manuscript

Plasmonic Properties of Regiospecific Core-Satellite Assemblies of Gold Nanostars and Nanospheres

A. Swarnapali D. S. Indrasekara,[a] Roney Thomas,[a] and Laura Fabris[*a,b]

Solution-based molecularly-mediated *bottom-up* assembly of gold nanostars and nanospheres in regiospecific core-satellite nanoarchitectures is reported. The controlled assembly is driven by coupling reactions in solution between small, rigid, Raman-active organic molecules bound to the surface of the nanoparticles, and leads to much narrower interparticle gaps than achievable with DNA-based assembly
10 methods. In the described system, gold nanostars with multiple sharp spikes, ideal for electromagnetic field enhancement, are used as the core particle onto which spherical satellites are assembled. Transmission electron micrographs show that the core-satellite structures assemble with <2 nm interparticle gaps and regiospecific binding of only one sphere per spike, and the process can be followed by monitoring changes in the surface enhanced Raman scattering (SERS) spectra of the Raman active
15 linkers. The assembled structures give rise on average to two orders of magnitude SERS signal enhancement per nanoparticle in comparison to their constituents, which can be attributed to the creation of SERS "hot spots" between the nanostar tip and the satellite sphere. Two dimensional finite element electromagnetic models show strongly confined electromagnetic field intensity in the narrow interparticle gaps of core-satellite assemblies, which is significantly enhanced in comparison to the constituent
20 nanoparticles, thus corroborating the experimental findings. Thus, the assemblies reported here can be envisioned as SERS-tags for imaging purposes as well as a model system for SERS-based chemical sensing with improved sensitivity.

Introduction

Design and *bottom-up* synthesis of plasmonic nanoparticles (NPs)
25 to sustain high electromagnetic field enhancements have become of significant interest in surface enhanced Raman scattering (SERS) in view of the possibility of fabricating highly enhancing substrates and imaging tags for analytical and biomedical applications. In these approaches, the intrinsic optical properties
30 of plasmonic NPs have been used to induce significant enhancements of the evanescent electromagnetic (EM) field in proximity to the NP surface and hence increase sensitivity. Of particular interest are locations called "hot spots", typical examples of which are sharp edges and corners or crevices in
35 single NPs, or intermetallic junctions in NP assemblies.[1-3] Many studies on anisotropic NPs such as nanorods, nanocubes, or nanoprisms provide evidence of their significant SERS enhancement ability compared to their isotropic counterparts.[3, 4] Recently, star-shaped nanoparticles (ST) have demonstrated
40 extraordinary field enhancement in comparison to other shapes of NPs.[5-7] Gold STs are composed of a small, spherical core and sharp protruding spikes, with a tunable characteristic surface plasmon resonance band that lies in the near infrared (NIR) region of the electromagnetic spectrum.[6, 8] The optical properties
45 of STs strongly depend on the morphology of the spikes (i.e. length, number, and tip curvature), wherein a large localized EM

field enhancement exists.[9-11] For this type of NP it has been observed that the surface plasmon resonance wavelength red shifts with longer and more numerous spikes,[9,10,12] and that,
50 according to the lightning rod effect,[13-16] a narrow radius of curvature of the tips results in higher electric field confinement at these locations, thereby leading to stronger enhancement.

Although large SERS enhancements have been predicted in proximity to the sharp spikes of STs, studies have shown that
55 those achievable within the gap region between the spike tip and a secondary SERS-enhancing substrate can be even stronger.[10] For instance, Alvarez-Puebla et *al.* have shown that when a Raman active molecule is carefully attached to the tip of the spikes of a ST, and sandwiched between the latter and a
60 plasmonic surface, a SERS enhancement of 2 orders of magnitude higher than that observed on isolated STs can be observed,[17] enabling the detection of analytes in the zeptomolar regime. This observation motivated us to study the local field enhancement within the gap regions in core-satellite systems
65 made of gold ST cores and spherical satellites. Recently, we have employed gold STs to develop a SERS sensing substrate with a 10^9 enhancement factor;[18] based upon this result we expected that a construct coupling the ST to other plasmonic nanoparticles could generate SERS substrates with further improved
70 enhancement properties. For these reasons, the goal of our work was to explore *bottom up* assembly protocols that would produce

core-satellite systems where to each tip of a gold ST one and only one gold nanospheres (SP) was covalently bonded with regiospecific selectivity.

Several approaches toward *bottom up* NP assembly have been reported to improve the optical properties of NPs. For example, Xu et *al.* have achieved the regiospecific assembly of plasmonic nanorods and nanospheres by exploiting the non-homogenous cetyltrimethylammonium bromide (CTAB) distribution at the sides and tips of the nanorods. In their approach they selectively functionalized the nanorods with aptamers, and induced sphere-rod assembly via DNA hybridization.[19] The core-satellite assembly of spherical NPs of different sizes has also been designed taking advantage of alkanedithiol-triggered NP assembly exploiting the selective adsorption of NPs on a glass substrate,[20] or by covalent binding of NPs via small bifunctional linkers such as p-aminothiophenol.[21] However, as we are interested in applying assembled NP constructs as SERS tags in biological systems, we needed to ensure that the stability and interparticle gaps of the assemblies, and hence the SERS "hot spots", could be retained under physiological conditions. Thus, it was necessary to design synthetic schemes to generate covalently linked assemblies with high stability even in physiological conditions. In our previous work, we have demonstrated that small, rigid, Raman active organic molecules can be employed to assemble spherical NPs in dimers with 1-2 nm interparticle gaps and well-defined, stable, and reproducible EM field enhancement for use as cell imaging tags.[22]

Herein, based on our prior successful results, we report on the core-satellite assembly of gold STs and gold SPs, which results in assemblies with well-defined interparticle distance, and increased SERS activity compared to the isolated constituents and to analogous nanostructures achieved employing oligonucleotide hybridization. Our strategy involves the formation of an amide bond between 4-aminothiophenol (ATP)-capped SP and 4-mercaptobenzoic acid (MBA)-capped gold ST via 1-ethyl-3-(3-dimethylaminopropyl)carbodiimide / N-hydroxysulfosuccinimide (EDC/sulfoNHS) coupling reactions and the consequent generation of a narrow interparticle gap. Compared to substrate-mediated assembly protocols, our approach is advantageous as it ensures that the assembly does not only take place on the non-tethered, solvent-exposed side of the ST. In the following sections, we will present the synthetic methods, the structural and optical properties of the as-assembled superstructures, and the supporting theoretical two dimensional finite element electromagnetic modeling (2D-FEEM) simulations identifying the positions of high EM field enhancement. In particular, we have exploited SERS to follow the assembly process, and hypothesize the applicability of these core-satellite assemblies as SERS tags for biological and medical imaging.

Experimental Section

Materials

All the reagents used for this study were purchased from Sigma Aldrich and used as received. Ultrapure MilliQ water was used for all the syntheses. Thiolated-methoxy PEG (MeO-PEG-SH) (MW= 5000 Da) was purchased from Nanocs Inc. EDC and sulfo-NHS were purchased from Pierce Biotechnology, Inc. All

the glassware was cleaned with aqua regia, rinsed multiple times with MilliQ water, and air-dried before use.

Nanoparticle Synthesis

Synthesis of spherical Au NPs

Citrate capped spherical Au NPs (SP) of 12 nm and 24 nm in diameter were synthesized according to a modified version of the Turkevich method.[31] Briefly, a solution of HAuCl$_4$ (25 mg) in MilliQ water (487.5 mL) was heated up to boil, followed by the addition of citric acid trisodium salt under stirring (1% wt., 9 mL and 12.5 mL for 12 nm and 24 nm SPs respectively). After 30 minutes of boiling, the solution turned orange/red and was allowed to cool to room temperature. Au NPs were purified by centrifugation at 10000 g for 60 min and 6000 g for 30 min for 12 nm and 24 nm SPs respectively.

Synthesis of star-shaped Au NPs

Gold nanostars (ST) were synthesized according to a modified version of the surfactant-free synthesis described by Vo-Dinh and coworkers.[12] Briefly, 20 μL of 1 N HCl and 25 μL of 15 nM citrate capped 12 nm SPs were added to 10 mL of 1 mM HAuCl$_4$ solution, and mixed thoroughly by stirring. 200 μL of 100 mM ascorbic acid and 400 μL of 3 mM AgNO$_3$ were then simultaneously added to the above mixture, gently stirred for 7 min, and purified by centrifugation at 3000 g for 15 min. The purified STs were resuspended in 10 mL of MilliQ water and refrigerated until further use.

Surface Functionalization of Nanoparticles with Raman Active Linker Molecules

SPs and STs were ligand exchanged with 4-aminothiophenol (ATP) and 4-mercaptobenzoic acid (MBA) respectively. These molecules act both as SERS reporters as well as linker molecules amenable to coupling reactions when exposed to EDC/ sulfo-NHS. NPs were mixed with the linker molecules and left overnight at room temperature, followed by purification via centrifugation. In particular, separate batches of STs capped with MBA (MBA-ST) were prepared at a NP:MBA molar ratio of 1:10000. SPs capped with ATP (ATP-SP) were prepared at a NP:ATP molar ratio of 1:300. NP suspensions capped with ATP were maintained at acidic pH while those capped with MBA were kept at basic pH to prevent the possible aggregation of NPs through hydrogen bonding. The relatively lower molar ratio employed for NP:ATP was selected because of the high aggregation rates induced in the presence of high ATP ligand density on the NP surface, and also to avoid the formation of aggregated assemblies during the EDC/sulfo-NHS coupling reaction.

Core-Satellite Nanoparticle Assembly by EDC/sulfo-NHS Coupling

EDC/sulfo-NHS coupling reactions were carried out in aqueous NP suspensions at pH 5.5-7.0 at room temperature. MBA-STs were mixed with EDC and sulfo-NHS (0.01 M, pH 7.0) at 1:10 and 1:20 molar ratio, respectively. After 1 min, the solution containing MBA-STs mixed with EDC and sulfo-NHS was added to 150 μL of 6 nM ATP-SPs, the reaction was allowed to proceed for 10 min, and was then followed by quenching through addition of 1 mg/mL of MeO-PEG-SH. The NPs were mixed to achieve

ST:SP molar ratios of 1:50, 1:100, 1:150, and 1:200. The assembled nanostructures were then purified by removing excess reagents and unreacted NPs via centrifugation at 3000 g for 15 min, and resuspended in 200 μL of MilliQ water.

Characterization of Core-Satellite Assemblies

The absorption spectra of the NP suspensions were measured on a Varian Agilent Cary 50 Bio-UV-Vis spectrophotometer. The morphology of the NPs was evaluated using a Topcon 002B transmission electron microscope, and size information was extracted using the Image J software.

All the Raman and SERS spectra were obtained using a Senterra (Bruker) Raman spectrometer. Samples were prepared for the analysis by placing a known volume of NP suspension on a silicon wafer. The SERS spectra were obtained using a 785 nm diode laser excitation (1 mW, spot size 2 μm) with two accumulations for 15 s acquisition time under a 50X objective. The SERS spectra and relative intensities presented here are the averages of three baseline-corrected measurements obtained at random places on the samples.

Electromagnetic Modeling

A two dimensional finite element electromagnetic modeling (2D-FEEM) study was carried out using the RF module of the Comsol Multiphysics software to obtain the optical field properties of STs and ST-SP assemblies at various symmetric and asymmetric configurations. A transverse magnetic (TM) polarized light (i.e., electric field polarized along the X-axis) was used to illuminate the structure. The 2D-FEEM model assumes no variation of the electric field in the third dimension, i.e., along the Z-axis. The optical analysis aids in providing a qualitative understanding of light-nanostructure interactions, such as the dependence of the electric field distribution and enhancement on (i) the number of spikes and the presence of absence of satellite SPs, (ii) the gap distance between the protruding spike and the attached SPs, and (iii) the electromagnetic coupling (EC) effect between the adjacent spikes of the STs, and the dependence of the field intensity profiles on the angle of incidence of the polarized light with respect to the ST-SP assembly geometry.

The physical dimensions, such as the diameters of the STs gold core, the dimension of the satellite SPs, the radius of curvature of the spike tip edge, and the length of the spikes, were chosen in the 2D-FEEM simulation to be similar to their respective experimental values (see section 2.1). The incident power was defined in terms of the magnitude of the electric ($|E|=1$ V/m) and magnetic fields. For accurate modeling, the characteristic impedance of the electromagnetic (EM) wave propagating through the medium (i.e. water) was taken into account and given by $|E|/|H| = 1/(\mu_0/(\varepsilon_0\varepsilon))^{1/2} = 248.3$ Ωs, where ε_0 and μ_0 are the dielectric permittivity and permeability of air and ε is the dielectric permittivity of water (i.e. 1.33). The wavelength-dependent optical constants of gold were obtained from E. Palik.[32]

Results and Discussion

Synthesis and Characterization of Precursor Nanoparticles

Monodisperse suspensions of SPs of 24 ± 2 nm in diameter were synthesized by citrate reduction of $HAuCl_4$, and characterized

monitoring the localized surface plasmon resonance mode centered at 520 nm in the UV-Vis absorption spectra (Fig. 1). STs were synthesized by a modified version of the surfactant-free, seed-mediated method first introduced by Vo-Dinh and coworkers.[12] With our modified protocol (see experimental section) we were able to allow the morphology evolution to reach thermodynamic equilibrium and hence synthesize ST with longer spikes and much sharper tip curvature (Figure 1).
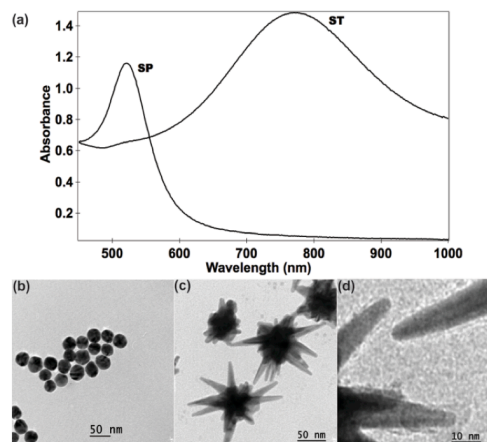

Fig. 1 (a) The absorption spectra of gold nanostars (ST) and nanospheres (SP). TEM micrographs of (b) SPs (c) STs, and (d) a closer view of a ST spike.

The gold STs produced have an average spherical core of 36 ± 3 nm in diameter and spikes of 40 ± 5 nm in length with tip curvature of about 3 ± 1 nm. The absorption spectrum of the ST is composed of two localized surface plasmon resonance modes: A shoulder peak around 520 nm corresponding to the spherical core resonance, and a second, much broader plasmon mode appearing at around 785 nm, which arises due to the sharp protruding spikes from the spherical core. The current protocol for the synthesis of STs is unable to ensure homogeneity in terms of the number of spikes per particle and the length of spikes, resulting in broad surface plasmon resonance modes, as evidenced in the absorption spectrum (Fig. 1a). Even though the synthesis of STs is not accompanied by surfactants, the SERS analysis shows the presence of ascorbic acid on the surface of the purified STs (Fig. S1), thus we hypothesize that ascorbic acid might provide colloidal stability for STs besides its role as a reducing agent.

Characterization of the Core-Satellite Assemblies

The ST-SP core-satellite assembly was carried out via a EDC/sulfoNHS coupling reaction between ATP-capped SPs and MBA-capped STs (**Scheme 1**). Citrate capped SPs and ascorbic acid-capped STs were ligand exchanged with ATP and MBA, respectively. The stoichiometric ATP concentration necessary to provide complete surface coverage of SPs resulted in aggregated structures, which can be attributed to the reaction of excess ATP on SPs with multiple STs. Instead, an amount of ATP sufficient to cover only 1/32 of the SP surface was found to work best for assembly purposes and lead to stable and well defined assembled nanostructures. The ligand exchange reaction solutions were maintained at pH~4 for the ATP-capped sample and pH~8 for the MBA-capped one in order to avoid hydrogen bonding-triggered

aggregation. Successful ligand exchange was confirmed via SERS analysis, monitoring the ensuance of the characteristic SERS signatures for 4-ATP and 4-MBA (Fig. S2). In addition, the lack of morphology changes, as observed from the TEM micrographs, was considered strong evidence that no NP aggregation had taken place prior to the assembly reaction.
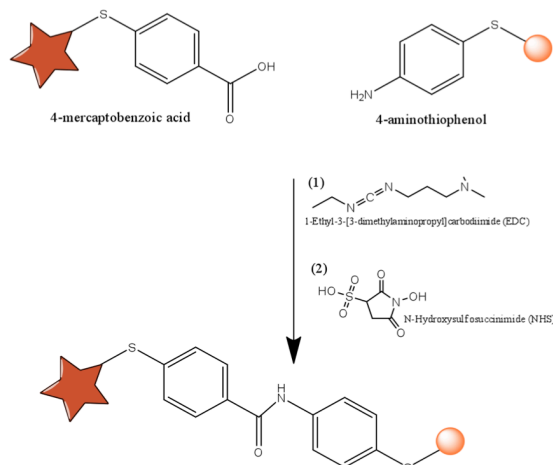
Scheme 1 Schematic representation of the EDC/sulfo-NHS coupling reaction that leads to core-satellite assembly between SPs and STs. Not drawn to scale

The optimum reaction time for the assembly was determined by quenching the coupling reaction at different time intervals (1-5 min at 1 min intervals, 10, 15, 20, and 30 min) via addition of thiolated, methoxy-terminated polyethylene glycol (SH-PEG-MeO). The surface-bound PEG molecules are intended to contribute toward steric repulsion between particles, and to effectively prevent further coupling. Based on absorption spectra and TEM micrographs, 10 min was found to be the ideal reaction time, as after that no significant changes were observed (Fig. 2). In addition to quenching the coupling reaction, PEG capping is also intended to provide colloidal stability, and to replace any unreacted ATP and MBA from the surface of the NPs. Being longer than ATP and MBA molecules, PEG molecules are expected to replace them through ligand exchange reactions at almost all the locations but the interparticle junctions, hence contributing to the simplification of the SERS analysis. By a semi-quantitative analysis, it was realized that the pegylation leads to the decline of SERS intensity of MBA-STs approximately by a factor of 10 upon (Fig. S3)

We also carried out a control reaction without EDC/NHS in order to confirm it as the driving force for ST-SP assembly. No significant assembly through electrostatic interactions between ATP-capped SPs and MBA-capped STs was observed (Fig. S4), and thus it can be concluded that the covalent coupling through EDC/NHS is necessary to stabilize NP-NS assemblies.
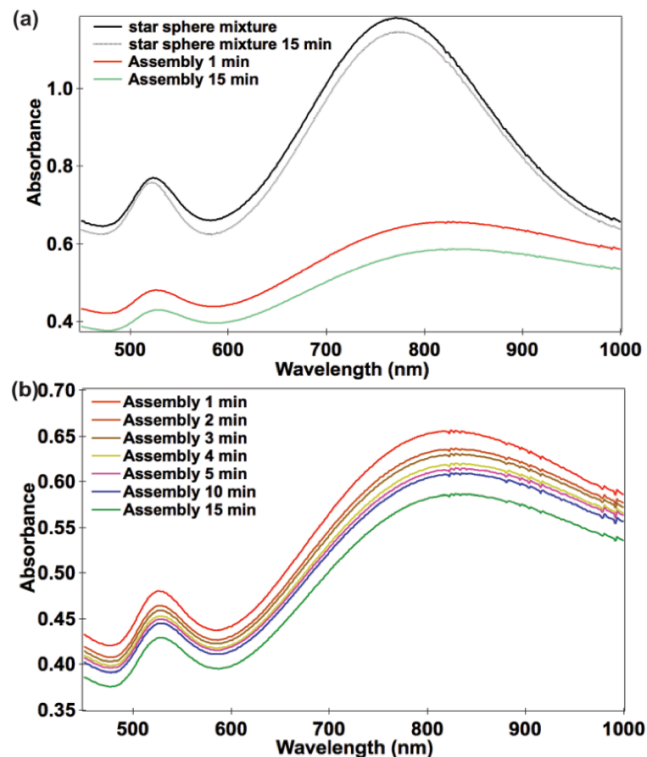

Fig. 2. The absorption spectral changes upon assembly are mediated by the EDC/sulfo-NHS coupling reaction between precursor NPs. UV-Visible spectra of (a) a mixture of STs and SPs with no coupling reaction, and (b) assembly reaction at different time intervals.

Upon assembly, significant modifications were observed in the absorption spectrum. As shown in Fig. 2, when no assembly reaction has taken place, the absorption spectrum presents collective localized surface plasmon resonance modes relevant to the precursor NPs where a peak at 520 nm for ATP-SP and a broad peak for MBA-ST around 785 nm are observed. Upon assembly, a large red shift of the ST plasmon mode toward an absorption maximum centered around 850 nm was observed while a ~5 nm red shift of the SP plasmon mode was observed. These peak shifts can be explained as due to the assembly-triggered plasmon coupling between NPs,[23, 24] and, more specifically, as the result of a narrow interparticle gap formation. According to our models (*vide infra*), new plasmonic modes should appear for NP assemblies at longer wavelengths, which are however difficult to identify experimentally due to the inherent structural inhomogeneity of STs that results in broadened plasmon peaks, which may mask any new plasmon modes (if present), and are difficult to deconvolute, especially in ensemble-averaged nanoparticle systems suspended in solution.

Fig. 3 shows the TEM images for the sample with ST:SP ratio equal to 1:50, which was chosen as it provided optimized assembly conditions and high yield of assemblies per sample. Statistical analysis of 30 assembled structures shows that, on average, there are three satellite SPs per core ST, and that to each ST spike one and only one SP is bound. However, the current protocol is not capable of achieving the exact placement of the SP

at the apex of the spike, resulting in SPs that are often offset from it by about 2 nm. In addition, the inability of the method to exactly couple each spike with a sphere can be attributed to the structural inhomogeneity of the ST, which present a number of 5 spikes varying between 5 and 10. However we have observed a preferential regiospecific assembly at or very close to the apex of the nanostar spikes. Our hypothesis is that the high-energy facets at the tips of the spikes are highly reactive in comparison to the rest of the locations on nanostars. Thus, more EDC activated 10 MBA molecules could be resided at the tips of the spikes, thereby increasing the probability for capturing nanospheres through EDC-NHS chemistry. Nonetheless, TEM micrographs provide evidence for effective core-satellite assembly and narrow interparticle gaps (< 2 nm), which is of fundamental importance 15 for the study of SERS enhancement and for the appearance of novel multipolar plasmonic modes. Core-satellite assembly was also carried out with nanospheres of 12 nm in diameter, and results are shown in Fig S5.
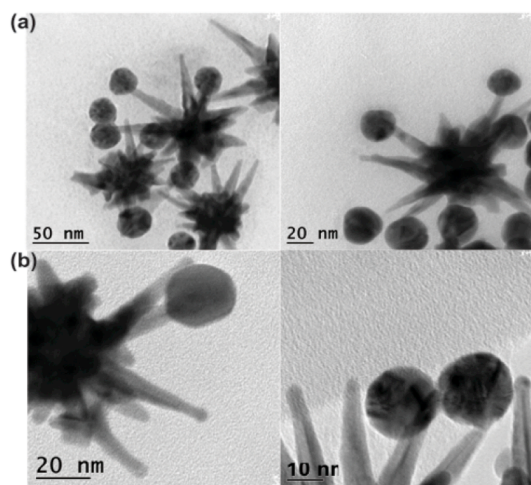

20 **Fig. 3** TEM micrographs show the assembly of SPs at or very close to the acute tip of the spikes of STs. TEM micrographs of (a) multiple assemblies per ST, and (b) closer views of assembly showing narrow interparticle gap (< 2 nm).

As shown in Scheme 1, the core-satellite assembly is driven by 25 the formation of an amide bond between ATP and MBA. Upon assembly, the linking moiety resides in the narrow (< 2 nm) interparticle gap, which is also a "hot spot", and thus experiences high field enhancement. In addition, because of the conjugated system resulting from the coupling of MBA and ATP, electron 30 delocalization is highly favoured, and can induce charge transfer processes leading to the appearance of novel vibrational modes. This can be observed experimentally in the SERS spectra of the core-satellite assemblies, which show significant changes in the spectral shifts as well as changes in the relative peak intensities in 35 comparison to the precursor NPs (Fig. 4).

In general, not only the SERS spectra show the characteristic vibrations of MBA and ATP with enhanced intensity because of the creation of "hot spots", but also new bands centered at around 700 cm^{-1}, 1763 cm^{-1}, 1250 cm^{-1}, and 1380 cm^{-1} can be observed, 40 which can be ascribed to the newly formed amide bonds.[25-27] The peak around 1763 cm^{-1} can be assigned to the amide I band (C=O stretch), which was not prominent in the MBA-STs, but

can become visible in the SERS spectra of assemblies owing to its default placement in SERS "hot spot" upon assembly. The 45 broad peaks around 1250 cm^{-1} and 1380 cm^{-1} can be assigned to the C-O stretching mode of the carbonyl group (in the amide bond), and the C-C/C-H b$_2$ vibrational modes respectively, which have been reported to appear due to chemical enhancement processes (i.e. due to charge transfer mechanisms).[28, 29] The 50 other vibrational modes characteristic of the amide bond (C-N bending, N-H bending) cannot be observed most likely due to the steric constraints that the molecules experience within the narrow interparticle gap. In addition, upon NP assembly, it can be clearly noticed that the enhancement of the peaks corresponding to C-H 55 vibrational modes (1180 cm^{-1} and 1481 cm^{-1}) is much higher compared to that of the aromatic ring vibrations (at 1077 cm^{-1} and 1586 cm^{-1}). This observation has also been reported by others, and explained as due to the signal enhancement through charge transfer mechanism.[29] The core-satellite assembly is mediated 60 by the amide bond formation between ATP and MBA thereby placing the newly formed Raman active molecular structure in the SERS "hot spot".[29] This might facilitate metal-to-molecule charge transfer in addition to other chemical enhancement processes, and thereby result in the observed SERS signal 65 enhancement. By considering all these spectral differences, it can be concluded that the core-satellite assembly has taken place through amide bond formation and that a narrow interparticle gap has been created.
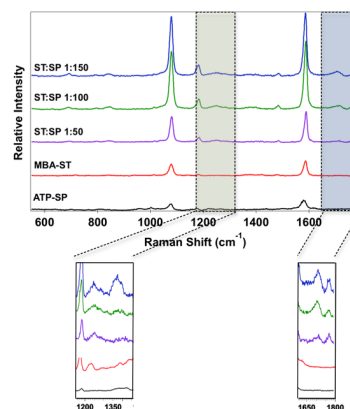

70 **Fig. 4** SERS spectral signature of assemblies in comparison to precursor NPs confirms that the ST-SP assemblies are mediated by amide bond formation. The appearance of new peaks due to the amide bond formation can be clearly observed in the 1200-1350 cm-1 and 1600-1800 cm-1 regions of the SERS spectra following assembly. SERS spectra were 75 acquired under 785 nm diode laser (1 mW, 15 s exposure, 2 accumulations).

To further demonstrate that the assembly process leads to the generation of narrow interparticle junctions, we calculated the SERS signal enhancement of the analyte (either MBA or ATP) on 80 NPs. The average SERS signal enhancement factor (EF) for the analyte on NP was calculated following equation:

$$EF = \frac{(I_{SERS} / N_{SERS})}{(I_{Raman} / N_{Raman})}$$

where I_{Raman} is the intensity of the Raman signal for the analyte under non-SERS conditions, I_{SERS} is the intensity under SERS

condition, and N_{Raman} and N_{SERS} are the number of probed analyte molecules under Raman and SERS conditions, respectively.[30] The average Raman intensity for 50 mM ethanolic MBA and ATP was considered for I_{Raman}. N_{Raman} was calculated as the number of MBA or ATP molecules present in the laser spot size (2 μm). In order to calculate N_{SERS} within the laser spot, it was assumed that a monolayer of analyte molecules (MBA or ATP) exist over the NPs. Knowing the number of moles of NPs (ST or SP) within the laser spot and the molar analyte (MBA or ATP) surface coverage on NPs, the number of probed analyte molecules was calculated using the following equation:

N_{SERS} = (number of moles of NPs probed × molar surface coverage of the analyte × Avogadro number)

Since STs have a significant structural inhomogeneity, for an accurate estimation of SERS EFs the calculations were carried out considering the amide-bonded ligand molecules as residing over the entire surface area of the assembly instead of only at the "hot spots". However, those residing at the SERS "hot spot", which are present in much smaller number, are the major contributors to the observed SERS signal. Therefore, considering all the analytes on the surface of the assembled structure for the calculation of EF leads to an underestimation of the actual EFs that can be achieved using core-satellite assemblies. The EFslisted in Table 1 show that the core-satellite assemblies give rise to a 2-orders of magnitude increase in the SERS EF relative to the precursor STs. In other words, core-satellite assemblies provide SERS EFs equal to 10^{10} while isolated STs provide a 10^8 enhancement. These results suggest that core-satellite assemblies, where SPs assemble at the tip of the ST spikes, provide higher SERS enhancements compared to those achievable in individual STs or SPs, which can be relevant if one wanted to employ these nanostructures as tags in SERS-based imaging applications.

Table 1. SERS EFs of precursor NPs and core-satellite assemblies calculated for the peak at 1582 cm^{-1}.

Sample	EF
MBA-ST	1×10^8
ATP-SP	1×10^4
ST: SP =1:150	0.5×10^{10}
ST: SP =1:100	1.5×10^{10}
ST: SP =1:50	5×10^{10}

Optical Simulations of the Core-Satellite Assemblies

Optical simulations using 2D-FEEM were carried out modeling STs as composed of a spherical gold core and protruding spikes both in the presence and absence of coupled satellite SPs. Theoretical simulations are important not only because they allow one to better understand the experimental results but also because they offer guidelines for further optimization of the assembly protocols, as they can predict the locations of highest field enhancement in relation to the wavelength of interest as it impinges on the nanostructure. TEM images of the core-satellite assemblies have shown that in all the assemblies observed the SP is located within 0.5 to 2 nm from the tip of the spike, hence a SP located at the arbitrary average distance of 1.28 nm from the tip of the ST spike was considered for simulation purposes.

Furthermore, TEM images have revealed that the SP is generally offset with respect to the axis bisecting the spike by a maximum of 2 nm, therefore the case of a SP shifted from that axis and at 1.28 nm away from the tip was also considered for optical analysis.

In all of the EM simulations, the core-satellite assemblies were simulated to obtain the electric field intensity ($|E|^2$) distribution at wavelengths between 400 and 1000 nm. It must be noted that all the $|E|^2$ plots also identify the electric field intensity enhancements since the incident field intensity ($|E_0|$) was assumed to be 1 V/m. A qualitative analysis of the $|E|^2$ spectrum in the region close to the spike's apex was carried out for gold STs without SPs and with symmetrically and asymmetrically arranged gold SPs. Integrated electric field intensity spectra along a 10 nm long vertical line, located at 1 nm from the tip (see the inset of. S6a), were obtained using 2D-FEEM, and evidence a maximum integrated $|E|^2$ at λ = 692 nm for the gold ST structure with a symmetric and an asymmetric SP located close to the spherical edge of the protruding spike. It was found that for the gold ST with SPs located symmetrically along the axis bisecting the spike, the maximum integrated $|E|^2$ is enhanced by a factor of ca. 19 compared to the case without SPs. In order to understand this phenomenon, $|E|^2$ plots at λ = 692 nm for different ST-SP configurations were obtained as shown in Fig. S6 b-d. Fig. S6b shows the electric field intensity plot for the gold ST structure without SPs, while Fig. S6c and d show field intensity plots for Au STs with symmetrically and asymmetrically arranged SPs with respect to the axis of the spike, respectively. Fig. S6b shows a highly localized electric field intensity concentrated near the spheroidal tip region of the protruding spike. The enhanced electric field intensity near the tip can be attributed to the excitation of the localized surface plasmons which resonate at λ = 650 nm (Fig. S6a). The excited plasmons are contributed primarily from the sharp tip of the protruding spike and partially from the gold core structure, resulting in a hybridized plasmon resonance near the tip of the ST spike.[10]

With the introduction of a gold SP in close proximity (~ 1.28 nm) to the spherical edge of the tip, hybridization between the plasmons excited by the spherical core, the sharp tip, and the SP occurs (Fig. S6c-d), leading to a large $|E|^2$ enhancement within the interparticle gap region, compared to the case without the SPs. This enhancement can be attributed to the strong EM coupling between the plasmon modes excited by the hybrid core-tip ST structure and the closely situated SP, which leads to a large red shift in the integrated $|E|^2$ peak in contrast to the ST without SPs. The effect of the change in the separation between the tip and SP will be discussed later in the section. Since the incident light is polarized along the X-axis, electric field intensities are symmetrically distributed with respect to the axis of the protruding spike when the SP is placed exactly at the center of the tip, while they are asymmetrically distributed in the case of a SP asymmetrically coupled to the ST with respect to the axis bisecting the tip. Furthermore, in the latter case, the EM coupling between the plasmons excited in the protruding tip and those in the SP is hindered, resulting in a reduced resonant peak in $|E|^2$ in the gap region between tip and SP. Thus, the peak $|E|^2$ enhancement for the asymmetric ST-SP structure is almost reduced by a factor of 2 compared to the peak magnitude of $|E|^2$

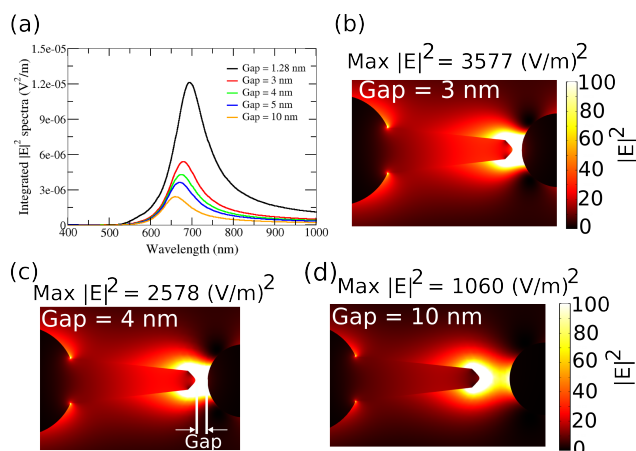obtained for the symmetric ST-SP structure.

Fig. 5 a) Change in integrated $|E|^2$ intensity measured along a line located 1 nm from the tip at increasing ST-SP gap size. (b), (c) and (d) depict $|E|^2$
5 intensities for a ST with a single protruding tip and a symmetric SP located at varying gap distances.

To prove the dependence of the electric field enhancement on the distance between the ST spike and the satellite SP, we carried
10 out distance-dependent 2D-FEEM simulations for the symmetric gold ST-SP structure. In a manner similar to what was described before, $|E|^2$ spectra were integrated along a 10 nm line situated 1 nm away from the apex while the gap between the tip of the ST and the symmetrically arranged SP was decreased from 10 nm to
15 1.28 nm, as shown in Fig. 5a. It shows an overall increase in electric field intensity with a maximum that red shifts from 655 nm to 690 nm as the gap decreases from 10 nm to 1.28 nm. Fig. 5b-d show $|E|^2$ plots with increasing gap separation (3 nm, 4 nm, and 10 nm) between the spherical tip of the spike and ST at λ =
20 692 nm. The EM coupling between the plasmon modes excited by the tip of the protruding spike and that of the closely situated SP becomes increasingly stronger with decreasing gap distance, resulting in an increased maximum $|E|^2$ within the spatial region between the tip and the SP. Careful observation of Fig. 5d reveals
25 that, as the gap increases, the plasmon mode supported by the symmetrically situated SP tends to decouple from the one supported by the tip of the protruding spike. However, the plasmon mode supported by the SP is very weak in comparison to that supported by the core-tip structure of the ST and, therefore,
30 contributes only negligibly towards the integrated $|E|^2$ spectrum. Hence, no prominent peak due to the plasmon mode excited by the SP was observed in the integrated field intensity plot shown in Fig. 5a. It was found that, for the structure with 3 nm gap between the tip and the SP (Fig. 5a), the simulated maximum
35 electric field intensity was 3 times larger than the structure with the gap distance of 10 nm.
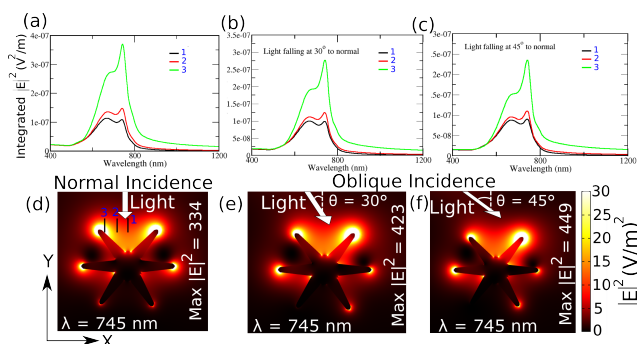

Fig. 6 Top panel: Integrated $|E|^2$ spectrum obtained along a 10 nm line situated at positions 1, 2, and 3 within the region between the second and
40 third protruding spikes as indicated by the solid black lines in (d) for the ST nanostructure illuminated along the normal (a) and oblique ((b),(c)) incident light. Bottom panel: $|E|^2$ plots at the resonant wavelength λ = 745 nm for the normal and oblique incident TM polarized light.

45 Theoretical investigations using 2D-FEEM were further employed to study the effect of the angle of incidence of the incoming radiation (normal and oblique) on the electric field distribution around a ST with six protruding spikes. For this study it is important to note that, because of the particular ST geometry
50 built for this model, which includes three C_2 axes of symmetry, two S_h and two S_v planes of reflection, the incoming light was assumed to impinge on the ST only from the top, but that the results for light incoming from the bottom can be obtained employing transformations along C_2, S_h, and S_v. As a result, the
55 lack of electric field enhancement around spikes 5 and 6 (see Figure 7 for numeration) observed in Fig. 6 can be explained and resolved invoking fundamental group theory rules. In the calculations, the STs were illuminated by light impinging at 30° and 45° from the normal, and the spatial distribution of the
60 electric field intensity enhancements was compared with the ST illuminated from a normally incident light. In a manner similar to what was described before, integrated electric field intensity spectra along 10 nm long vertical lines situated between the second and third spikes, as shown by the solid black lines in Fig.
65 6d, were obtained for light impinging along the normal and at 30° and 45° from it.

Fig. 6a-c show integrated $|E|^2$ spectra obtained along the black solid lines situated at the fixed position marked as 1, 2, and 3 in Fig. 6d for a ST illuminated with light impinging along the
70 normal (a), at 30° (b), and at 45° (c). The figures indicate peaks in the integrated field intensity obtained along the line situated in the region nearest to the spherical tip of the third spike. Fig. 6d–f show the electric field intensity plots at λ = 745 nm, which correspond to maxima in integrated $|E|^2$ spectra shown in green in
75 Fig. 6a–c. For the reasons discussed before, the plasmon modes appear to be strongly excited by the spherical tip of the second and third protruding spikes of the gold ST and weakly excited by the tips of the other spikes. It is evident from the field intensity plots from the bottom panel that the plasmon modes supported by
80 the tips of spikes 2 and 3 produce highly localized field intensity close to the edge of the tips, which significantly decreases away from it, as indicated by the red and black curves in Fig. 6a–c.
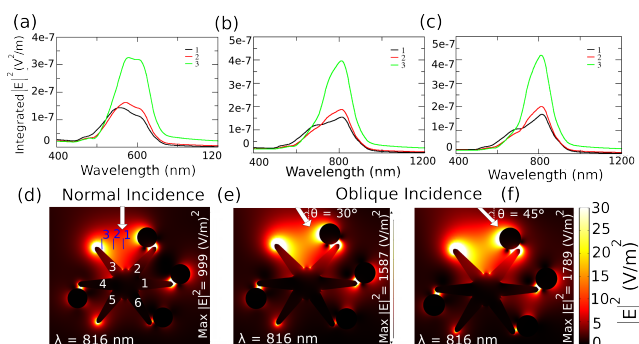
Fig. 7 Top panel: |E|2 spectra integrated along a 10 nm solid line at positions marked as 1, 2, and 3 in (d) for the gold ST-SP assemblies illuminated from a normal (a) and oblique ((b), (c)) incident light. Bottom panel: Electric field intensities at $\lambda = 816$ nm, which correspond to the peak intensity for the gold ST-SP assemblies illuminated from light incident at 30° and 45° from the normal, respectively.

By careful observation of Fig. 6e and f one can observe how $|E|^2$ in the vicinity of the tip of the third spike is reduced as the angle of incidence increases from 30° to 45°. Conversely, a much more intense electric field appears to be localized by the tip of the second spike. The above phenomenon can be attributed to a decreased spatial EM interaction between the incident electric field and the surface of the spherical tip, which results in a weakly excited plasmon mode by the tip and, therefore, a smaller electric field intensity cross-section. In contrast, for the tip of spike 2, a larger spatial EM interaction results in a strongly excited plasmon mode, and therefore in a larger field intensity cross-section. Thus, it may be suggested that for a wider range of incident angles, a TM-polarized light impinging on a ST with six spikes protruding from its core, would induce one or more spherical tips of the spike to support strongly excited plasmon modes creating a "hot spot" in the vicinity of the spherical curvature of that tip.

A similar orientation-dependence study was also carried out on ST-SP assemblies. Based on the TEM images reported in Fig. 3, which show that SPs can be both symmetrically and asymmetrically bonded to their respective spikes, and that an arbitrary number of SPs can be bound to the spikes, for simulation purposes we built a gold ST with six protruding spikes and four SPs situated arbitrarily at 1.5 nm from the apex of spikes 1, 2, 4, and 6. In a manner similar to what was described before, integrated $|E|^2$ spectra along the solid lines at positions marked as 1, 2, and 3 in Fig. 7d, were obtained for the ST-SP assembly structures illuminated by a normally and obliquely incident light, as shown in Fig. 7a-c.

For the normally incident light illuminating the ST-SP assembly, the maxima in the integrated $|E|^2$ spectra at $\lambda = 745$ nm and 815 nm in Fig. 7a are red-shifted in comparison to the peaks at $\lambda = 675$ nm and 790 nm of the integrated $|E|^2$ spectra for the gold ST without SPs (Fig. 6a), which indicates the presence of strong EM field coupling between the core and the satellites. In addition, Fig. 7a-c indicate that the magnitude of the peak in the integrated $|E|^2$ spectra corresponding to $\lambda = 815$ nm is significantly enhanced at angles of incidence of 30° and 45° in comparison to the normally incident light, and can be explained as due to the higher degree of alignment of the incoming light with the interparticle axis that intersects the "hot spot".

Fig. 7d-f show the electric field intensity plots for the gold ST-SP assemblies illuminated from a normally and obliquely incident light at resonant wavelength, $\lambda = 816$ nm, which corresponds to a maximum in the integrated intensity spectra. It can be seen from the figures that the presence of a gold SP in close proximity to the tip of a protruding spike generates a plasmon mode that is strongly confined in the gap region between the tip and the spike. Additionally, the SP excites a dipole-dipole plasmon oscillation, which is more prominent for the gold SP situated near the tip of spike 2, as shown in the figures. For the light impinging diagonally a stronger EM coupling between the plasmons excited by the tip of the third spike and the plasmonic dipole resonant mode supported by the SP near spike 2 was achieved in comparison to the ST-SP assembly illuminated by a normally incident light (Fig. 7d). This leads to a larger spatial distribution of the enhanced $|E|^2$ in the region between the second and third spike resulting in an increased peak intensity for the $|E|^2$ spectra, as shown in Fig. 7b and c.

Taken together, the results of the 2D-FEEM simulations provide a theoretical basis that corroborates the experimental results described above. In a gold ST with six or more spikes evenly spaced around a spherical core, a longitudinally polarized electric field induces intense field localization in close proximity to the spherical tip of the protruding spike, which is however accompanied by the presence of a field envelope in the region surrounding the tips, albeit of lower intensity. This result may become of significance in the field of SERS, implying that, although the placement of a Raman reporter at the tips of the ST would ensure maximum signal enhancement, a smaller contribution to the signal could be provided by other reporters bound to the ST surface. The 2D-FEEM results also showed that the $|E|^2$ intensity in proximity of a tip bound to a satellite SP is larger, by a factor of 19, than that calculated in the absence of satellites, confirming the SERS EF values that were conservatively estimated in the experiments, which are equal to 10^8 for STs and 10^{10} for core-satellite systems.

Conclusions

In summary, the proposed *bottom up* assembly method could represent a valid alternative to the current lithographic and DNA-based approaches toward the creation of highly enhancing nanoparticle junctions. Our molecularly-mediated assembly route led to nanoarchitectures with SERS enhancement factors two orders of magnitude higher than those provided by the constituent nanostars, which could prove important to study the assembly of nanoparticle junctions at the single-particle single-molecule level. As evidenced by TEM, these assemblies are constituted by a single nanostar core and several spherical satellites, where only one satellite is bound to the tip of a protruding spike. Even though the results are promising, ensuring that each spike is bound to an individual satellite is challenging. Hence, to improve upon our current protocol, we are currently investigating solvent-mediated, site-specific ligand exchange reactions, and the different chemical reactivity of the thermodynamically stable crystallographic facets present on the stars, to increase the regiospecificity during the assembly process. Overall, the SERS enhancement factors experimentally measured on the core-satellite assemblies are well supported by 2D-FEEM simulations of the electric field enhancement, and make the herein described

superstructures a promising SERS tag candidate, especially for highly sensitive SERS-based imaging approaches. Based on these results, we are currently exploring synthetic protocols for tip-to-tip ST assembly in order to further improve plasmon hybridization. We anticipate that the described method will enable us to produce functional assemblies that could be extensively used in SERS sensing and imaging applications that go beyond proof-of-concept and model studies.

Notes and references

a Department of Materials Science and Engineering, Rutgers University, 607 Taylor Road, Piscataway NJ, 08854, USA.
Fax: 732 445 3258; Tel: 848 445 5606; E-mail: lfabris@rci.rutgers.edu
b Institute for Advanced Materials Devices and Nanotechnology, Rutgers University, 607 Taylor Road, Piscataway NJ, 08854, USA

† Electronic Supplementary Information (ESI) available: [details of any supplementary information available should be included here]. See DOI: 10.1039/b000000x/

[1] J. E. Millstone, S. Park, K. L. Shuford, L. Qin, G. C. Schatz, C. A. Mirkin, *J. Am. Chem. Soc.* **2005**, *127*, 5312-5313.
[2] H. Wu, C. Kuo, M. H. Huang, *Langmuir* **2010**, *26*, 12307-12313.
[3] C. J. Murphy, T. K. Sau, A. M. Gole, C. J. Orendorff, J. Gao, L. Gou, S. E. Hunyadi, T. Li, *J Phys Chem B* **2005**, *109*, 13857-13870.
[4] E. Hao, G. Schatz, J. Hupp, *J. Fluoresc.* **2004**, *14*, 331-341.
[5] C. Hrelescu, T. K. Sau, A. L. Rogach, F. Jackel, J. Feldmann, *Appl. Phys. Lett.* **2009**, *94*, 153113-153113-3.
[6] C. G. Khoury, T. Vo-Dinh, *J. Phys. Chem. C* **2008**, *112*, 18849-18859.
[7] L. Rodriguez-Lorenzo, R. A. Alvarez-Puebla, F. J. Garcia de Abajo, L. M. Liz-Marzan, *J. Phys. Chem. C* **2010**, *114*, 7336-7340.
[8] A. M. Fales, H. Yuan, T. Vo-Dinh, *Langmuir* **2011**, *27*, 12186-12190.
[9] F. Hao, C. L. Nehl, J. H. Hafner, P.Nordlander, *Nano Lett.* **2007**, *7*, 729-732.
[10] R. Alvarez-Puebla, L. M. Liz-Marzan, F. J. Garcia de Abajo, *J. Phys. Chem. Lett.* **2010**, *1*, 2428-2434.
[11] C. L. Nehl, H. Liao, J. H. Hafner, *Nano Lett.* **2006**, *6*, 683-688.
[12] H. Yuan, C. G. Khoury, H. Hwang, C. M. Wilson, G. A. Grant, T. Vo-Dinh, *Nanotechnology* **2012**, *23*, 075102.
[13] J. Lee, B. Hua, S. Park, M. Ha, Y. Lee, Z. Fan, H. Ko, *Nanoscale* **2014**, *6*, 616-623.
[14] B. Saute, R. Narayanan, *Analyst* **2011**, *136*, 527-532.
[15] I. Baginskiy, T. Lai, L. Cheng, Y. Chan, K. Yang, R. Liu, M. Hsiao, C. Chen, S. Hu, L. Her, D. P. Tsai, *J. Phys. Chem. C* **2013**, *117*, 2396-2410.
[16] *Surface Enhanced Raman Spectroscopy. Analytical, Biophysical and Life Science Applications.* S. Schlücker, Ed. Wiley-VCH: Weinheim, 2010.
[17] L. Rodriguez-Lorenzo, R. A. Alvarez-Puebla, I. Pastoriza-Santos, S. Mazzucco, O. Stephan, M. Kociak, L. M. Liz-Marzan, F. J. Garcia de Abajo, *J. Am. Chem. Soc.* **2009**, *131*, 4616-4618.
[18] A. S. D. S. Indrasekara, S. Meyers, S. Shubeita, L. C. Feldman, T. Gustafsson, L. Fabris, *Nanoscale* **2014,** *6*, 8891-8899.
[19] L. Xu, H. Kuang, C. Xu, W. Ma, L. Wang, N. A. Kotov, *J. Am. Chem. Soc.* **2012**, *134*, 1699-1709.
[20] J. H. Yoon, J. Lim, S. Yoon, *ACS Nano* **2012**, *6*, 7199-7208.
[21] N. Gandra, A. Abbas, L. Tian, S. Singamaneni, *Nano Lett.* **2012**, *12*, 2645-2651.
[22] A. S. D. S. Indrasekara, B. J. Paladini, D. J. Naczynski, V. Starovoytov, P. V. Moghe, L. Fabris, *Adv. Healthcare Mater.* **2013**, *2*, 1370-1376.
[23] W. Chang, B. A. Willingham, L. S. Slaughter, B. P. Khanal, L. Vigderman, E. R. Zubarev, S. Link, *P. Natl. Acad. Sci. USA* **2011**, *108*, 19879-19884.
[24] Z. Nie, A. Petukhova, E. Kumacheva, *Nat. Nanotechnol.* **2010**, *5*, 15-25.
[25] C. Gullekson, L. Lucas, K. Hewitt, L. Kreplak, *Biophys. J.* **2011**, *100*, 1837-1845.
[26] D. Kurouski, T. Postiglione, T. Deckert-Gaudig, V. Deckert, I. K. Lednev, *Analyst* **2013**, *138*, 1665-1673.
[27] E. Podstawka, Y. Ozaki, L. M. Proniewicz, *Appl. Spectrosc.* **2004**, *58*, 570-580.
[28] T. Chen, H. Wang, G. Chen, Y. Wang, Y. Feng, W. S. Teo, T. Wu, H. Chen, *ACS Nano* **2010**, *4*, 3087-3094.
[29] X. Hu, T. Wang, L. Wang, S. Dong, *J. Phys. Chem. C* **2007**, *111*, 6962-6969.
[30] E. C. Le Ru, P. G. Etchegoin, *MRS Bull.* **2013**, *38*, 631-640.
[31] J. Turkevich, P. C. Stevenson, J. Hillier, *Discuss. Faraday Soc.* **1951**, *11*, 55-75.
[32] E. D. Palik, Handbook of Optical Constants of Solids. Elsevier Science & Tech, Ed. 3, 1985.